ORIGINAL ARTICLE

lajss.org©
Latin American
Journal of Solids
and Structures

www.lajss.org

Mechanical Performance and Structural Integrity of 3D-Printed Polylactic Acid in Tensile Testing: Influence of Hole Fabrication Technique and Process Parameters

Enes Kalyoncu[ab*], **Birgül Aşçıoğlu Temiztaş**[a], **Berna Bolat**[a], **Ali Can Kaya**[c]

[a]Department of Mechanical Engineering, Faculty of Mechanical Engineering, Yildiz Technical University, Yildiz, Besiktas, Istanbul, Türkiye. Email: eneskalyoncu@outlook.com, birgul@yildiz.edu.tr, balpan@yildiz.edu.tr
[b]Department of Machinery and Metal Technologies, Istanbul Gelişim University, Avcilar, Istanbul, Türkiye.
[c]Department of Mechatronics Engineering, Turkish-German University, Sahinkaya Caddesi 86, Beykoz, Istanbul, Türkiye. Email: alican.kaya@tau.edu.tr

*Corresponding author

https://doi.org/10.1590/1679-7825/e8775

Abstract

This study presents a systematic investigation of the tensile behavior of FFF-printed PLA specimens, with a specific emphasis on the role of hole fabrication methods—post-drilled versus integrated printed holes—on structural integrity. Unlike prior works that primarily addressed raster orientation and infill effects, this research isolates the influence of hole manufacturing techniques under standardized ASTM D638 and D5766 testing. Stress concentration factors (Kt) were calculated using classical analytical expressions, and their limitations for anisotropic FFF parts are acknowledged and further discussed in the Results and Discussion section. The results revealed that, although raster angle and infill density affected overall strength, the decisive factor was the method of hole generation: post-drilled holes consistently outperformed printed-hole counterparts in tensile resistance and failure behavior. Microscopic analysis confirmed that printed holes introduced interlayer misalignment and shell–infill discontinuities, accelerating crack initiation. These findings demonstrate that hole geometry alone is insufficient to guarantee mechanical reliability, and that the fabrication method of stress concentrators must be considered a critical design parameter in FFF applications.

Keywords

Fused Filament Fabrication (FFF), Drilled vs. Printed Holes, PLA, Stress Concentration Factor, Tensile Strength,

Graphical Abstract

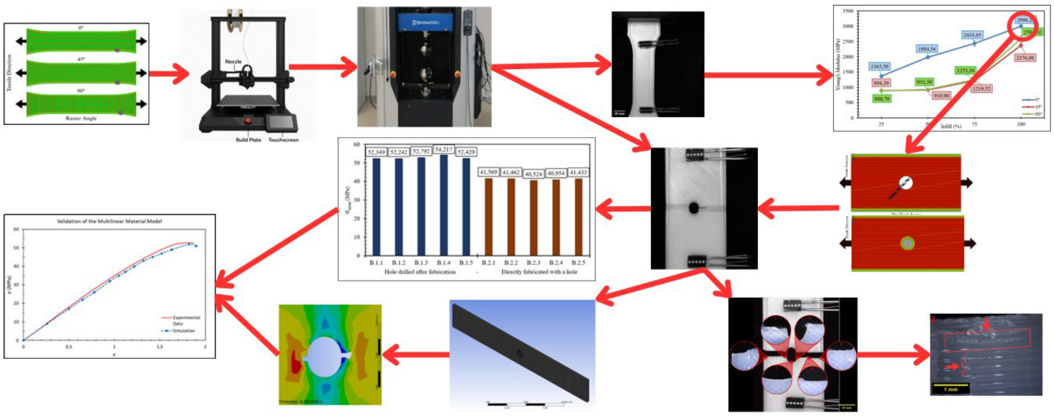

Received July 22, 2025. In revised form October 23, 2025. Accepted October 24, 2025. Available online October 27, 2025.
https://doi.org/10.1590/1679-7825/e8775

1 INTRODUCTION

Additive manufacturing (AM) offers a unique approach to conventional methods by facilitating the layer-wise integration of diverse materials within a single build process. This developing technology provides significant advantages, particularly for manufacturing parts with intricate geometrical features (Love et al., 2014; Badiru, 2017). Among AM techniques, Fused Filament Fabrication (FFF) stands out due to its low cost, ease of use, and accessibility for industrial and research purposes. Other methods, such as Laminated Object Manufacturing (LOM), Stereolithography (SLA), and Selective Laser Sintering (SLS), are also commonly employed depending on application-specific requirements (Mohamed et al., 2015).

Prior studies on FFF-manufactured thermoplastics have focused on elastic properties and failure resistance. Although stiffness and modulus are well documented, insights into fracture mechanics remain limited (Choudary et al., 2023). The mechanical outcomes of FFF-printed components are strongly dependent on the selected process parameters, a topic that has been extensively reviewed in the literature (Mohamed et al., 2015). Among the most critical factors is the raster orientation, which has been shown to induce significant anisotropic behavior and directly govern the ultimate tensile strength of PLA parts (Yao et al., 2020). Another key parameter, infill density, is directly correlated with the component's stiffness and overall load-bearing capacity (Badiru et al., 2017). Experimental studies confirm that raster angle and infill density significantly influence stiffness and tensile strength, while standardized testing according to ASTM D638 is commonly applied to ensure consistency in specimen geometry and layer thickness (Anand Kumar & Narayan, 2019).

The performance consistency of FFF-manufactured components is closely linked to hardware configuration and the selection of printing settings. Variations in process parameters during fabrication can significantly affect the structural attributes of PLA, a topic comprehensively covered in several reviews (Solomon et al., 2020; Liu et al., 2019). Building conditions determine the final mechanical strength, and numerous studies have isolated the effects of individual settings. For example, parameters related to the internal structure, such as infill percentage and layer width, have a direct and measurable correlation with the mechanical properties of the final part (Moradi et al., 2023; Tanveer et al., 2019). Other operational settings, like print speed, also play a critical role in the mechanical performance and integrity of the component (Lorkowski et al., 2025). Therefore, achieving optimal structural performance often requires a holistic approach to parameter optimization, considering the interplay between these multiple factors (Abeykoon et al., 2020).

Defects found during the 3D printing process might compromise the final item quality, particularly in terms of mechanical dependability (Abeykoon et al., 2020). Therefore, the primary focus of modern research has become improving print accuracy, material use efficiency, and cycle time by precisely controlling process variables (Khosravani et al., 2022).

Polylactic acid (PLA), a highly processable and biodegradable polymer, has been extensively employed in AM over the past decade. Its applications encompass sectors such as healthcare (Farah et al., 2016), aerospace (Yao et al., 2020), industry, civil engineering (Talagani et al., 2015) and food (Lipton et al., 2015). Among the thermoplastics applied in FFF techniques, PLA is identified due to its relatively moderate melting point, biocompatibility, and environmental benefits. However, PLA also has limitations, including insufficient temperature resistance and moisture absorption, which might limit mechanical stability (Lipton et al., 2015). Constant efforts in design improvement and simulation-based evaluation—such as finite element analysis (FEA)—seek to reduce failure causes, including stress buildup and interlayer cracking (Talagani et al., 2015).

Triyono et al. (2020) examined how different nozzle diameters (varying in the interval of 0.3–0.6 mm) affected the porosity and tensile strength of PLA components made with FFF. Their findings showed that the 0.5 mm nozzle generated the most consistent mechanical response, thereby improving density and interlayer adhesion; deviations to lower or larger diameters caused structural inconsistencies because of insufficient raster spacing. Akhoundi and Behravesh (2019) examined the mechanical response variations due to changes in the print path and infill configuration of PLA components generated by FFF. Their results support the significance of print-related parameters on structural efficiency printing parameters in line with the parametric analysis carried out here. Dave et al. (2020) conducted a comprehensive factorial experiment looking at tilt, raster width, and layer thickness. Attained at a 0° raster angle, with a raster path of 500 µm and a deposition layer thickness of 200 µm (Triyono et al., 2020), the maximum tensile strength reported in their work was 36.37 MPa.

The mechanical response of FFF-printed PLA is anisotropic, primarily due to the influence of raster orientation on stiffness and tensile strength. Strength and elasticity change markedly with filament angle, highlighting the directional dependency of printed parts (Albadrani, 2023; Yao et al., 2019). Complementary studies have captured three-dimensional variations in elastic and yield properties, and these works show that isotropy cannot be inferred from a single Poisson's ratio value; rather, anisotropy arises from the directional dependence governed by raster orientation (Dai et al., 2020; Li et al., 2024).

The role of void morphology in ductile fracture, as reported by dos Santos et al. (2022), is conceptually relevant to the study of hole effects in FFF-printed PLA. In addition, key process variables including nozzle temperature, deposition rate, and layer thickness play a critical role in determining both the surface finish and mechanical strength of FFF-printed components, as highlighted by Bergonzi et al. (2024). Moreover, the structural response of printed geometries varies depending on loading direction and internal design, as evidenced by the recent findings presented by Luo et al. (2023).

Raj et al. (2018) demonstrated that specimens with 75% infill of PLA had an ultimate tensile capacity of 48.66 MPa and a modulus of elasticity measured at 3355.12 MPa. Their findings underlined the critical influence on the mechanical response of infill densities and layer thickness. Moreover, they found that although Poisson's ratio was hardly affected by printing speed, it greatly affected the directional strength attributes.

Yao et al. (2019) investigated how layer height affects mechanical properties and found that, due to decreased interlayer adhesion, thicker layers typically produce lower strength. Brounstein et al. (2020) emphasized that structural voids and interlayer discontinuities in FFF-printed composite materials serve as loci for failure initiation. Their research using digital microscope data showed how poor interlayer adhesion and micro void development influence the structural uniformity and performance stability of produced components.

Farah et al. (2016) observed that PLA components typically exhibit tensile strength ranging from 50 to 70 MPa and report an elastic modulus near 3 GPa. They underscored the significance of tailoring printing settings to alleviate anisotropic behavior and enhance mechanical integrity. An analogous environmental study demonstrated that PLA components underwent a mass loss of approximately 6.22% following four weeks of soil exposure, with degradation continuing over time.

Zhao et al. (2019) investigated the structural behavior and shape-altering tendencies for PLA parts in relation to angular raster configurations from 0° to 90° and different deposition heights spanning a thickness range of 0.1 to 0.3 mm. Their investigation indicated that raster orientation improved stiffness and strength; however, higher layer thickness led to diminished mechanical performance due to insufficient interlayer bonding.

Mira et al. (2024) examined the role of dimensional compactness in determining failure durability of PLA and other thermoplastic materials. They observed that neither internal void formation nor part geometry significantly influenced the results of failure tests.

Guessasma and Belhabib (2022) investigated the impact of varying interior geometries and material loading ratios, focusing on how carbon fiber addition alters PLA's structural features. Among the evaluated geometries—gyroid, zigzag, and cross—the gyroid configuration, when paired with elevated infill loading, demonstrated enhanced tensile strength (27 MPa) and stiffness (399 MPa). These findings emphasize the significance of internal design in structural improvement and optimization.

Lubombo and Huneault (2018), PLA specimens with the same density were produced using 1 and 3 perimeters, and their mechanical performance was compared. According to the study, adding more perimeter paths increased strength and modulus between 30% to 84%. This enhancement is linked to the alignment of perimeter strands with the primary stress axis, facilitating improved load transfer capability. In particular, using three perimeters exhibited a more ductile and durable structural behavior regarding structural stiffness and failure resistance. However, the literature indicates optimal tensile strength is generally attained by 4 to 5 perimeters. Beyond this threshold, additional increases yield no further mechanical advantages and may result in negative consequences. These disadvantages include increased component weight and production time, incompatibility with infill structures, material waste, and the risk of deviating from the optimum design by concentrating the load distribution on the outer shell. It has been emphasized that a controlled increase in the number of perimeters positively affects mechanical performance; however, when increased excessively, it can negatively affect structural efficiency (Chokshi et al., 2022; Szczepanik and Nikiel, 2020).

While the effects of process parameters on the tensile properties of solid (un-notched) FFF parts are well documented, the failure behavior of components with geometric discontinuities such as holes remains a less explored area. Most existing studies on notched FFF parts treat the hole as an ideal geometric feature, often applying classical stress-concentration theories without accounting for the fabrication method of the hole itself. This leaves a significant gap in the literature regarding whether a hole created through subtractive post-processing (i.e., drilling) leads to a different structural response compared to a hole that is AM as an integrated feature (i.e., printed-in). This distinction is critical, as the toolpath generation and filament deposition around a printed hole may introduce microstructural discontinuities that act as premature failure sites.

To address this gap, the present study experimentally examined the mechanical performance of FFF-printed PLA specimens fabricated under ASTM D638 and D5766 standards. In the first phase, dog-bone specimens were produced with four infill densities (25%, 50%, 75%, 100%) and three raster orientations (0°, 45°, 90°), and the configuration yielding the highest elastic modulus was identified. In the second phase, perforated plates were prepared according to ASTM D5766 by two distinct methods—post-drilled and directly printed holes—and comparatively evaluated. Stress concentration factors (K_t) and stress distributions around the hole were derived from the experimental data, enabling a direct comparison of the effects of hole-forming technique on mechanical behavior and ultimate failure.

2 MATERIALS AND METHODS

2.1. 3D Printing Setup and Specimen Fabrication Strategy

The samples were produced with industrial-grade PLA filament using a Creality CR-10 Smart Pro 3D printer. A user-based optimization of the printing parameters was performed to ensure that the printouts were as close as possible to the designed dimensions. The extrusion width was set to 0.50 mm and the extrusion multiplier (flow rate control) to 91% to produce the print at the targeted dimensions. This adjustment was critical for minimizing the dimensional deviations from the CAD model, ensuring that the parts were printed as close as possible to the targeted dimensions. These special settings were applied manually via slicing software.

In addition, the layer thickness was determined to be 0.2 mm to ensure homogeneous and reproducible properties of the samples. It is reported in the literature that the reduction in tensile strength observed in PLA prints is often attributed to increased layer thickness (Rafiee et al., 2025). The specimen geometry was designed based on the ASTM D638 Type III standard. This type is recommended for rigid plastics with a nominal thickness of 4 mm, consistent with our design. Different geometries defined by ASTM D638 (Type I–IV) are known to influence the tensile properties of FFF-printed polymers. Laureto and Pearce (2018) demonstrated that Type IV specimens can yield up to 17% higher tensile strength than Type I, and that vertically printed Type IV specimens exhibit nearly 48% lower strength than their horizontal counterparts. Such findings confirm that specimen geometry directly affects reported values. Nevertheless, the use of Type III provides a standardized and consistent baseline for evaluating raster orientation and infill density as the primary variables in this study. Three layers were used on the top and bottom surfaces, the outer shells (perimeter) were set as 3 lines, and an inside-out printing strategy was preferred (Lubombo and Huneault, 2018). All samples were produced using the same brand of PLA filament with constant printing parameters and at room temperature. To ensure the reproducibility and consistency of the experimental results, all specimens were produced using a fixed set of printing parameters optimized for the employed printer and material (Table 1). These values are not universal defaults but correspond to the settings specifically adjusted in this study to achieve reliable print quality.

Table 1 Basic 3D printer parameters for sample production.

Print Parameters	Value
Extrusion temperature	200°C
Print speed	80 mm/s
First layer print speed	40% * Print speed
Table temperature	60°C
Movement speed between X/Y axes	60 mm/s
Movement speed in Z axis	20 mm/s
Nozzle diameter	0.40 mm
Raft	No

All specimen dimensions, including thickness and width, were measured at multiple positions following ASTM D638 and ASTM D5766 standards. Uniaxial tensile tests were conducted on a Shimadzu AGX-V (Kyoto, Japan) universal testing machine, which features a 100 kN load cell with ±0.5% force accuracy and integrated high-resolution measurement capability. Axial deformation was monitored in real-time using the TRViewX optical extensometer with marker-tracking functionality embedded within the system. Additionally, a 2-megapixel CCD camera was used during tensile testing to visualize and characterize the surface deformation behavior of the specimens. All mechanical testing procedures were conducted under ambient laboratory conditions (22 °C).

The applicable standards defined the tensile loading rates: 5 mm/min for specimens prepared according to ASTM D638 and 2 mm/min for specimens fabricated following ASTM D5766 (ASTM D638, 2016; ASTM D5766, 2019). Figure 1 illustrates the apparatus and experimental configuration utilized in this investigation: (a) the Creality 3D CR-10 Smart Pro printer employed for specimen manufacturing, (b) the Shimadzu AGX-V universal testing machine, and (c) a representative image of a PLA specimen during the uniaxial tensile test. For reproducibility, the technical specifications and manufacturer data of the PLA filament used in this study are summarized in Table 2.

Table 2 Properties of the PLA filaments used in fabrication (manufacturer datasheet).

Feature	Value
Filament Diameter (mm)	Ø 1.75
Table Temperature (°C)	60-80
Printing Temperature (°C)	190-210
Density (g/cm^3)	1.25

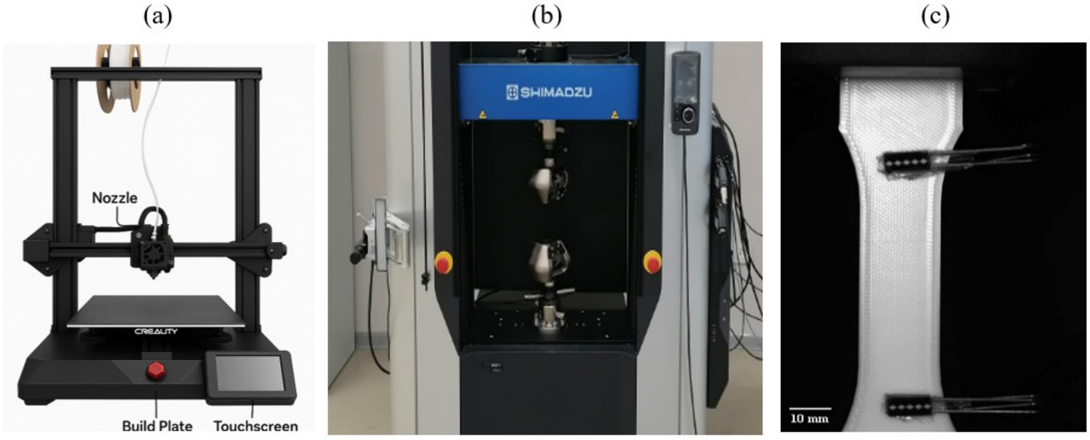

Figure 1 a) printer used for specimen production; b) tensile testing machine; c) tensile test of a 3D printed specimen.

2.2. Specimen Grouping and Design According to Raster Orientation and Infill Density

In the first phase of the study, the mechanical response of PLA samples produced via 3D printing was evaluated considering varying infill levels (25%, 50%, 75%, and 100%) and print path angles (0°, 45°, and 90°). Figure 2a also illustrates the presence of perimeter walls, which contribute to the overall strength of the parts. Thus, the layup does not correspond to an ideal unidirectional composite, as the shell–infill interaction plays a significant role in the mechanical response. Throughout testing, the directional arrows on both sides of every specimen show the direction of the applied tensile load. Sixty PLA specimens, fabricated using the FFF method, were examined to understand how these parameters impact the mechanical characteristics of the material. The specimen geometry was designed in a commercial CAD software package according to the ASTM D638 Type III standard and was exported as a high-resolution .STL file. This file was subsequently processed for printing using standard slicing software to generate the required G-code based on the parameters in Table 1 (Figure 2b). Five specimens were generated for every pair of infill ratio and orientation in the experimental design using a two-factor complete factorial experimental design.

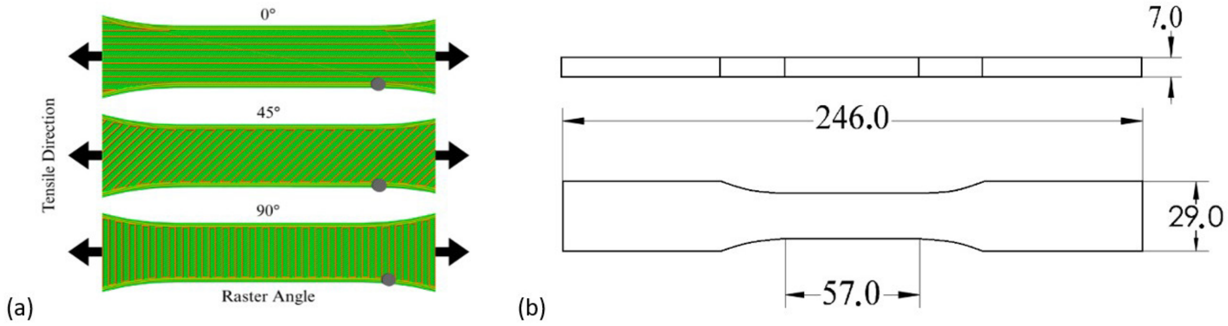

Figure 2 (a) Schematic illustration of PLA specimens showing raster orientations (0°, 45°, 90°) and perimeter walls (green) relative to the tensile loading direction. (b) Technical drawing of ASTM D638 Type III specimen geometry (dimensions in mm).

Linear infill was used as an infill pattern. 0° raster-oriented specimens were produced parallel to the loading direction, and 90° oriented specimens were produced perpendicular to the tensile direction. To minimize variability during production, each sample was printed by placing it individually in the center of the printing table.

2.3. Mechanical Evaluation of Perforated PLA Specimens Based on Hole Fabrication Method

The second phase of the research explored how the drilling technique influenced stress concentration around the hole. The mechanical response of the specimens featuring holes produced through distinct fabrication strategies was comparatively analyzed.

Perforated specimens were fabricated in accordance with ASTM D5766 using the highest-strength configuration determined in Phase 1 (0° raster, 100% infill). Ten specimens were prepared by two methods: (i) five printed with built-in holes and (ii) five printed solid and then drilled at a spindle speed of 1200 rpm. The specimen geometry followed the D5766 dimension (L = 250.0 mm, W = 36.0 mm, d = 6.0 mm, t = 4.0 mm). The tensile loading direction is indicated for both manufacturing techniques in Figure 3.

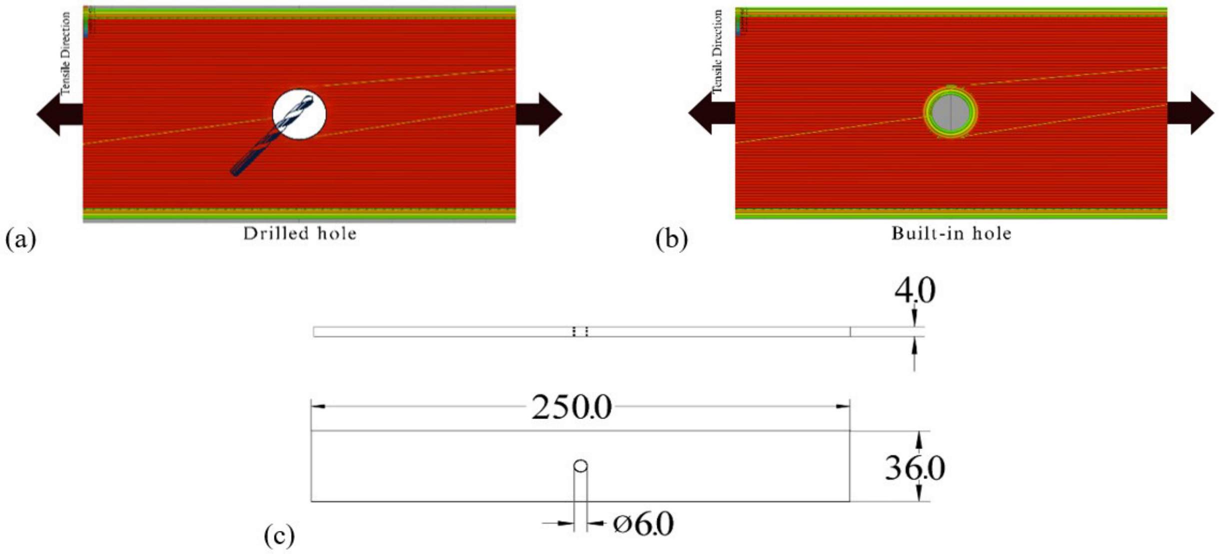

Figure 3 (a) Specimen with a post-process drilled hole; (b) specimen with an as-printed built-in hole; (c) technical drawing of the ASTM D5766 compliant specimen with all dimensions shown in millimeters (mm)

2.4. Analytical Assessment of Stress Concentration Around Holes (Kt)

The stress concentration factor (K_t) describes the local amplification of stress that occurs when the applied force increases the stress in structures with geometric discontinuities, such as holes. In classical continuum mechanics, this factor quantifies the ratio of the maximum theoretical stress at the discontinuity to the nominal stress (σ_{nom}) in the reduced cross-section for an idealized, isotropic material (Young and Budynas, 2002; Pilkey et al., 2020). Figure 4a illustrates the theoretical stress distribution, and Figure 4b shows the corresponding stress flow lines, illustrating how the load path is redirected around the hole.

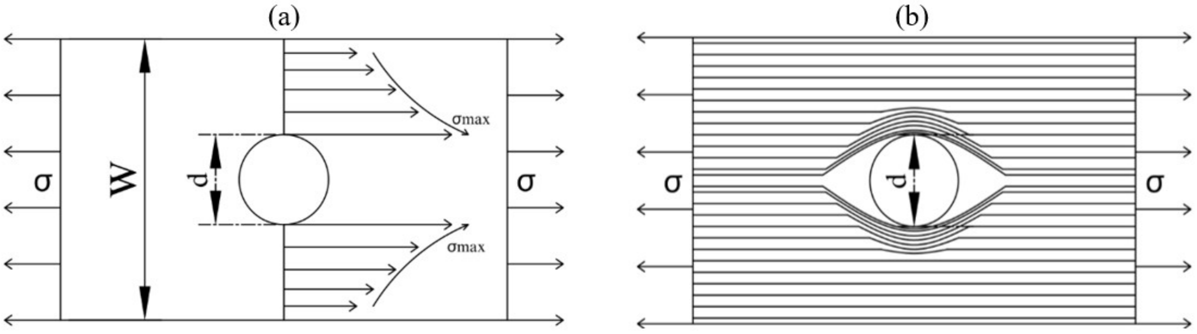

Figure 4 Stress analysis around a circular hole: (a) Stress distribution; (b) stress flow lines illustrating load-path redirection.

In calculations without taking stress concentration into account, the σ_{nom} which is obtained only on the basis of the reduced net cross-section due to the hole, presents an average value and does not reflect the actual stress state at the hole boundary. For a linear elastic and isotropic plate of finite width (width >> dimension) containing a central circular hole, the theoretical Kt can be calculated using the classical expression below [42], [43]

$$K_t = 3 - 3.14(\frac{d}{W}) + 3.667(\frac{d}{W})^2 - 1.527(\frac{d}{W})^3 \qquad [1]$$

where d is the diameter of the circular hole (mm), and W is the width of the specimen (mm). In the calculations, the average d/W ratios of B1 (drilled holes) and B2 (additively manufactured with built-in holes) specimens were determined as 0.167 and 0.158, respectively. Using Equation [1], the corresponding theoretical K_t values were calculated as approximately 2.57 (B1) and 2.59 (B2).

It is critical to recognize the limitations of this classical approach when applied to FFF-printed PLA. As established in the literature, such parts exhibit significant anisotropic behavior due to their layer-wise architecture. K_t reported here is a geometric stress-concentration baseline from the classical isotropic formula; it is not intended to represent manufacturing-induced anisotropy in FFF-printed PLA.

This geometry-dependent formula does not account for process-induced microstructural variations or defects associated with the hole fabrication method (i.e., post-drilling versus direct printing). Consequently, although the analytical K_t yields nearly the same nominal value for drilled and printed-in specimens (2.57 vs. 2.59) due to their identical geometry, the actual stress distribution and failure response can differ substantially. This discrepancy highlights that the classical K_t is not an exact predictor of the local stress state for these materials.

Therefore, this study uses K_t only as an idealized geometric baseline. This provides a reference against which the failure-governing effects of anisotropy and, more importantly, the manufacturing technique can be comparatively assessed, positioning the experimental σ_{nom} (presented in Section 3.2) as the most meaningful indicator of performance.

2.5. Numerical Validation and Simulation Setup

Numerical analyses in this study were conducted through the Explicit Dynamics module of FEA. The simulations modeled flat rectangular PLA plates with a centrally located circular hole of 6 mm diameter, in accordance with the ASTM D5766 standard. Each specimen had dimensions of 150 mm (length), 20 mm (width), and 4 mm (thickness) as defined by the standard.

The geometry was constructed to precisely match the specimens previously produced for experimental testing. The PLA material was defined using the Multilinear Isotropic Hardening (MISO) model, based on experimentally obtained stress–strain data. This allowed the simulation of plastic deformation behavior beyond the elastic limit. The material model was recalculated to align with the experimental results and was implemented in FEA as a stress–strain data table. Unloading was set to linear elastic; monotonic loading to failure means this choice does not affect the results.

During the simulation, a gradually increasing displacement load was applied to the loading direction was defined parallel to the X-axis, while the left end surface was constrained using a Fixed Support boundary condition. A low loading rate was applied to minimize dynamic effects, allowing for a quasi-static analysis of the time-dependent deformation behavior. The ratio of kinetic energy (KE) to internal energy (IE) was monitored during the explicit dynamics simulations and remained below 5% throughout the loading process, thereby validating the quasi-static assumption (Kim et al., 2014).

The model was discretized using SOLID185 3D solid elements within a three-dimensional domain. A hex-dominant mesh was generated using the Patch Conforming method, and local triangular facets were introduced around the hole to capture the curved geometry and maintain element quality during refinement. Mesh quality indicators such as skewness and aspect ratio were monitored and confirmed to remain within acceptable limits. A mesh sensitivity analysis with element sizes of 1.0 mm, 0.5 mm, and 0.2 mm was performed, and the 0.5 mm provided the best accuracy–cost trade-off, and adding local triangular facets near the hole did not change the stress fields.

To validate the accuracy of the defined material model, a comparison was conducted between the experimentally obtained stress–strain data and the recalculated stress–strain curve used in the FEA simulations. The validation was performed using drilled specimens with a central hole, since these were also employed in the experimental program. Specifically, the B1 configuration with a post-drilled hole, 0° raster orientation, and 100% infill density was selected for this purpose. Accordingly, the FEA geometry was created to replicate this drilled open-hole specimen. As shown in Figure 5, the implemented MISO accurately captured the material's behavior, especially beyond the elastic region. The good agreement between the two curves confirms that the model is suitable for simulating the plastic deformation behavior of PLA under tensile loading.

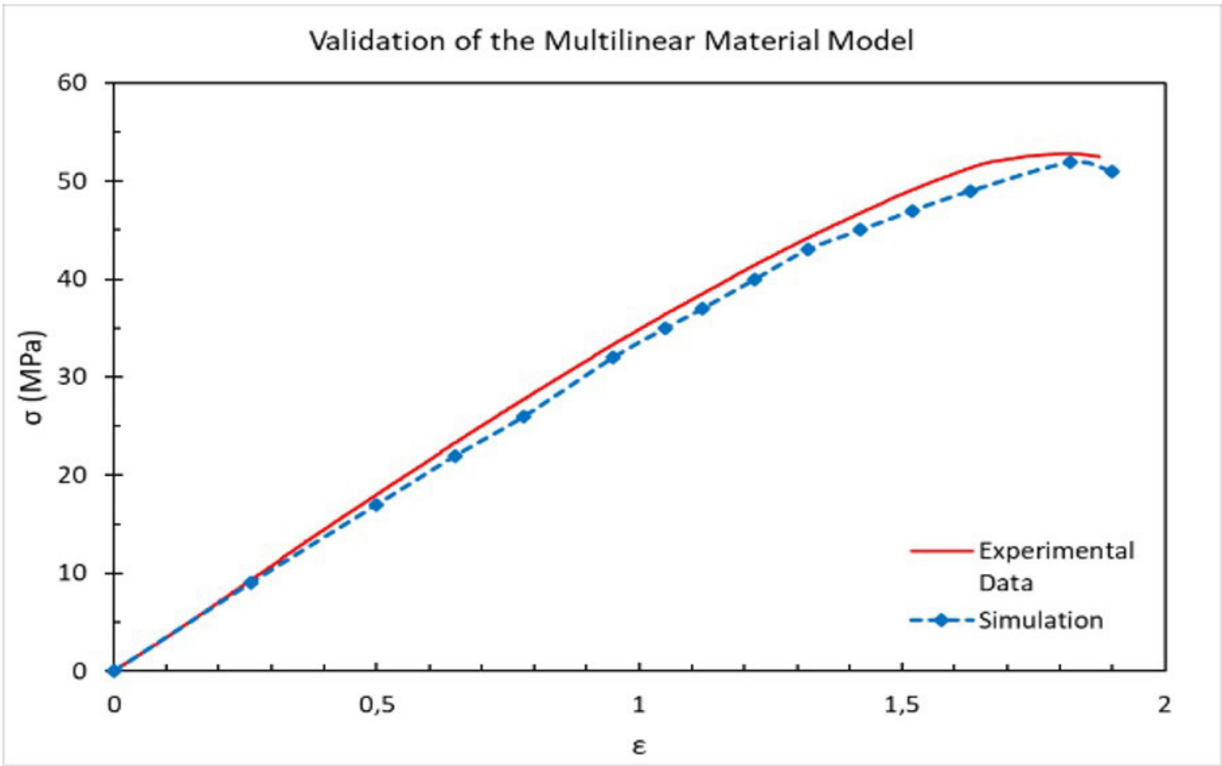

Figure 5 Comparison of the engineering stress–strain curves obtained from the experimental tensile test and the finite element simulation, used for the validation of the numerical model.

3 RESULTS

2.6. Combined Effect of Infill Density and Raster Orientation on Tensile Behavior

The mechanical test outcomes, including ultimate tensile strength (UTS) and Young's modulus, corresponding to each parameter configuration, are detailed in Table 3. These results were obtained from the tensile testing of 60 specimens, which were fabricated and tested according to the methods described previously (see Section 2). Specimens were fabricated with various raster orientations (0°, 45°, and 90°) and infill densities (25%, 50%, 75%, and 100%). For each parameter set, results were averaged over five individual specimens to ensure statistical reliability. In this study, specimens were tested with raster orientations of 0°, 45°, and 90°.

As shown in Table 3, Young's modulus values differ significantly with raster orientation (0°, 45°, 90°), confirming the anisotropic nature of FFF PLA. This means that the isotropic assumption behind the analytical K_t formula is limited, and orthotropic formulations would be required for exact predictions. Therefore, in this work the analytical K_t is used only as a geometric baseline, while the anisotropic material response is captured experimentally and numerically.

Tensile evaluations of PLA samples generated with different internal fill percentages and raster orientations yield mechanical performance results shown here. In Figure 6 and Figure 7, the data points represent the mean values of five experimental results obtained for each combination of raster orientation and infill density. The standard deviations for each mean are indicated by small black bars. The fact that the standard deviation values calculated for each series are below 1 supports the high consistency of the measurements and the reliability of the experimental data. Therefore, the reliability and statistical robustness of the data obtained are highlighted in the assessment of structural behavior of these series.

Specimens printed in the 0° direction achieved the highest strength due to the extruded filaments aligned along the loading path. The 0° specimen with 100% infill densities had approximately 103% higher tensile strength (39.050 MPa vs. 19.193 MPa) than the same direction specimen with 25% infill rates. Specimens printed in the 45° direction showed 30% lower tensile strength compared to the 0° specimens because the load-bearing filament trace were not fully aligned with the loading axis. The weakest tensile performance was observed in specimens fabricated at 90°, where poor interlayer adhesion resulted in the lowest strength. At 100% infill, the tensile strength of the 90° specimen was approximately 54% lower than that of the 0° specimen.

Table 3 UTS and Young's modulus results of PLA specimens produced at different raster angles and infill rates.

Infill (%) & Raster Angle (°)	Ultimate Tensile Strength (MPa)			Young's Modulus (MPa)		
	0°	45°	90°	0°	45°	90°
%25	19,002	10,787	12,274	1365,80	962,18	923,55
	18,988	11,065	12,037	1386,95	921,85	889,27
	18,180	10,662	11,883	1344,05	913,97	826,45
	20,070	11,573	12,088	1386,70	863,31	883,17
	19,726	11,411	12,071	1344,00	878,42	881,50
%50	27,140	10,206	12,410	2012,80	898,88	922,90
	30,589	9,738	12,497	2012,60	896,74	940,89
	27,407	11,426	12,477	2026,60	960,75	938,64
	29,910	11,256	12,456	1942,10	863,18	940,37
	29,943	11,762	12,847	1928,60	934,95	914,17
%75	32,558	12,856	17,160	2566,50	1201,10	1212,80
	34,353	13,305	17,032	2470,90	1190,90	1186,80
	33,157	13,445	17,598	2524,50	1265,50	1274,00
	35,412	15,462	17,187	2396,60	1292,30	1300,70
	36,280	14,934	17,476	2342,60	1147,80	1292,50
%100	38,587	30,164	17,046	2930,60	2381,30	2647,70
	39,439	30,502	18,674	2971,80	2507,00	2479,60
	39,125	29,313	18,833	3017,20	2358,20	2626,20
	39,417	30,828	17,359	3037,60	2302,90	2676,10
	38,683	30,001	18,146	3033,50	2339,80	2493,00

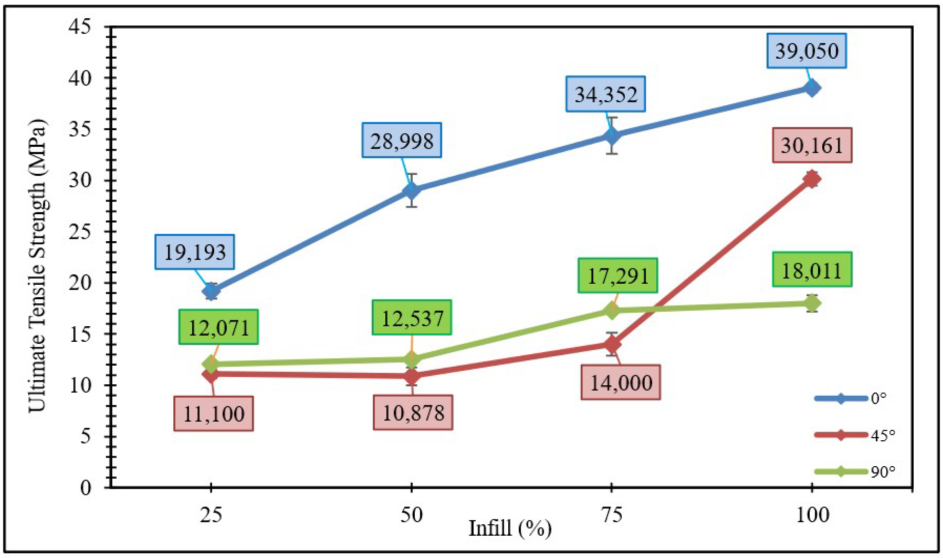

Figure 6 Influence of Infill Ratio and Raster Configuration on UTS.

Among the tested groups, specimens oriented at 0° and printed with 100% infill demonstrated the highest Young's modulus, reaching 2998.14 MPa. This represents a 120% increase compared to the 25% infill group, which showed a modulus of 1365.50 MPa. On the other hand, a 45° orientation led to approximately 20% lower stiffness, presumably due to the oblique filament paths arrangement that limited effective load transfer. The 90° specimens exhibited a comparatively high modulus although displaying the lowest tensile strength. Despite poor interlayer adhesion, this apparent disparity can be elucidated by the material's capacity for elastic deformation before failure. The 0° orientation yielded the highest modulus, while the 45° and 90° orientations resulted in significantly lower stiffness, consistent with prior reports by Yao et al. (2019) and Zhao et al. (2019).

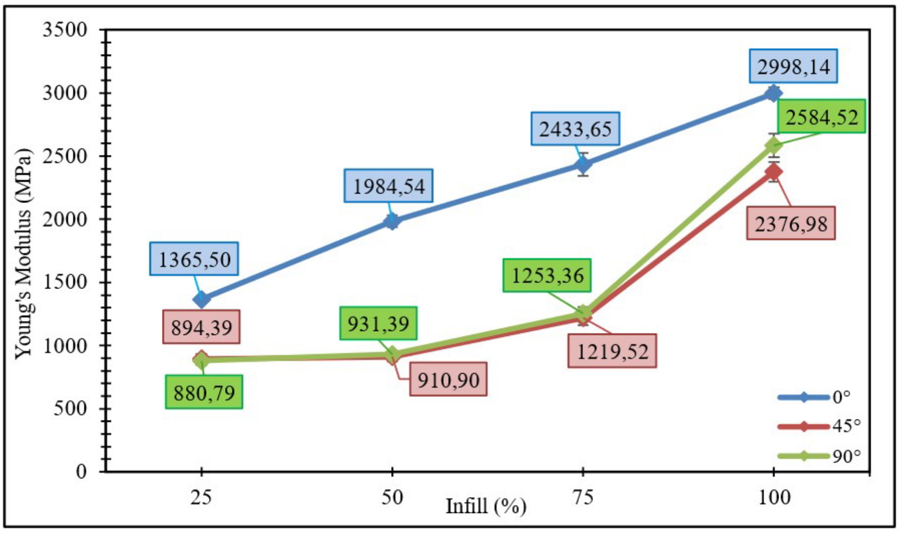

Figure 7 Young's Modulus & Infill Graphic.

2.7. Influence of Hole Formation Technique on Failure Behavior and Stress Distribution

Using the highest-strength configuration (0° raster, 100% infill), perforated specimens were fabricated in accordance with ASTM D5766 (Figure 3). Five specimens were printed with built-in holes (B2 series), and five were drilled after printing (B1 series) at a spindle speed of 1200 rpm.

Figure 8 compares the nominal stresses (σ_{nom}) of the individual specimens from both fabrication methods. The results clearly reveal a consistent performance gap between the drilled (B1) and printed-in (B2) configurations.

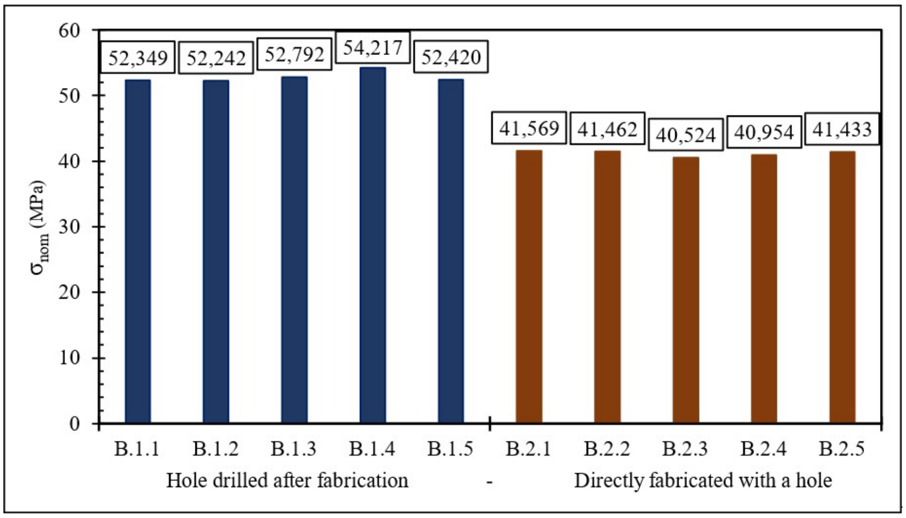

Figure 8. σ_{nom} for drilled (B1) and printed-in (B2) hole specimens. Bars represent individual specimen results, mean ± SD values are indicated above each group.

The drilled B1 series exhibited significantly higher strength, achieving an average $\sigma_{\mathrm{nom}}$of 52.8 ± 0.8 MPa, indicating strong statistical reliability and uniform mechanical behavior. This superior performance is attributed to the preserved filament continuity and microstructural integrity around the drilled holes, which minimized local stress raisers and improved load transfer across layers.

In contrast, the printed-in B2 series yielded a much lower average $\sigma_{nom}$of 41.2 ± 0.5 MPa. These reduced values are associated with process-induced layer disruptions, internal voids, and imperfect filament fusion around the as-printed holes. The observed performance degradation in B2 specimens was consistent across all samples, underscoring that the hole formation technique (rather than geometric stress concentration effects) plays a dominant role in governing the structural reliability of FFF-printed PLA parts.

2.8. Analysis of Microscopic Damage Features in Drilled and Printed PLA Specimens

In order to better understand the underlying causes of the mechanical behavior observed in the previous section, a microscopic investigation was conducted focusing on failure initiation and propagation in the B1 and B2 specimens. Although microscopic examinations were performed on multiple specimens, B.1.4 and B.2.5 were selected as representative cases due to their consistent structural features and clear visualization of characteristic failure mechanisms.

Figure 9 shows the sequential failure process in a PLA specimen under tensile load with post-drilled holes. The specimen displayed regular deformation behavior as the applied force changed from 6416 N to 6461 N (corresponding to a σ_{nom} range of 43.98–45.01 MPa). The red arrows indicate crack initiation points, propagation directions, and stress concentration zones observed during testing.

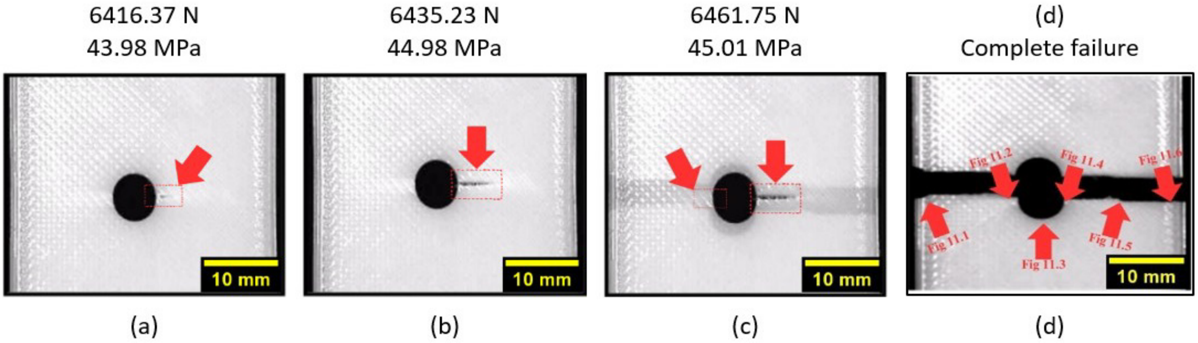

Figure 9 Sequential images showing crack initiation and propagation around the drilled hole in PLA specimen under tensile loading: (a) crack initiation, (b) intermediate propagation, (c) advanced propagation, (d) crack region formation.

To better understand the crack propagation characteristics observed in Figure 10, microscopic evaluation of the drilled B1 specimens was conducted. Crack initiation occurred in the area of stress concentration near the geometrical discontinuity of the hole. This amplified local stresses and triggered initial failure in that region, consistent with a brittle-like failure mode where failure began close to the peak load. The narrow load range indicates brittle-like failure initiating near peak load.

In Figure 9a, the crack initiation is clearly observed at the lower-right edge of the drilled hole. This region corresponds to the point of σ_{max} concentration under tensile loading, consistent with the geometry-induced weakness. In Figure 9b, the crack extends further from the initiation site and propagates horizontally across the outer shell region. The uniform filament paths alignment and strong interfacial bonding in this zone appear to have slowed down sudden propagation, causing a steady progression of the crack front. In Figure 9c, an additional crack appears to initiate near the opposite side of the drilled hole, rather than being a direct continuation of the primary crack path. This suggests the presence of independent stress concentrations at both sides of the hole, possibly due to the local stress field or slight asymmetries in material structure. In Figure 9d, complete failure of the specimen is evident. The crack path has fully traversed the narrow section, forming a continuous and nearly straight path. The clean break and absence of secondary crack branching indicate that the failure path mode was dominated by stress concentration rather than interlayer decohesion or uncontrolled microstructural irregularities.

To further explore the structural characteristics underlying the failure behavior of the B1 specimens, microscopic observations from both cross-sectional and top-down perspectives further clarified the failure behavior. The resulting images are presented in Figure 10 and Figure 11, respectively.

In the microscope image presented in Figure 10, the drilled region appears structurally intact, with a regular hole shape and continuous shell–infill integration. To provide a clearer understanding, Figure 11 illustrates the cross-sectional and top-down views, respectively, confirming the absence of significant interfacial defects in drilled specimens.

Figure 11 further elaborates the detailed microstructural features of the drilled hole. Region 1 in Figure 11 shows a well-organized and continuous infill pattern (red rectangle) with strongly bonded paths, suggesting good cohesion. Region 2, the upper-right side of the drilled hole is depicted, corresponding to the maximum tensile stress region (σ_{max}) observed in Figure 9c. Region 3 highlights the center of the drilled hole, where the surface exhibits consistent contact marks from drilling, suggesting localized compressive deformation. Region 4 captures the upper-left edge of the drilled hole, suggesting a clean shear contour, while adjacent printed roads remain well aligned. Region 5 illustrates the shell–infill transition with strong bonding. Finally, Region 6 presents the upper-right region, where extruded filament alignment is mostly regular, although minor inter-extruded filament gaps are visible, reflecting localized stress redistribution.

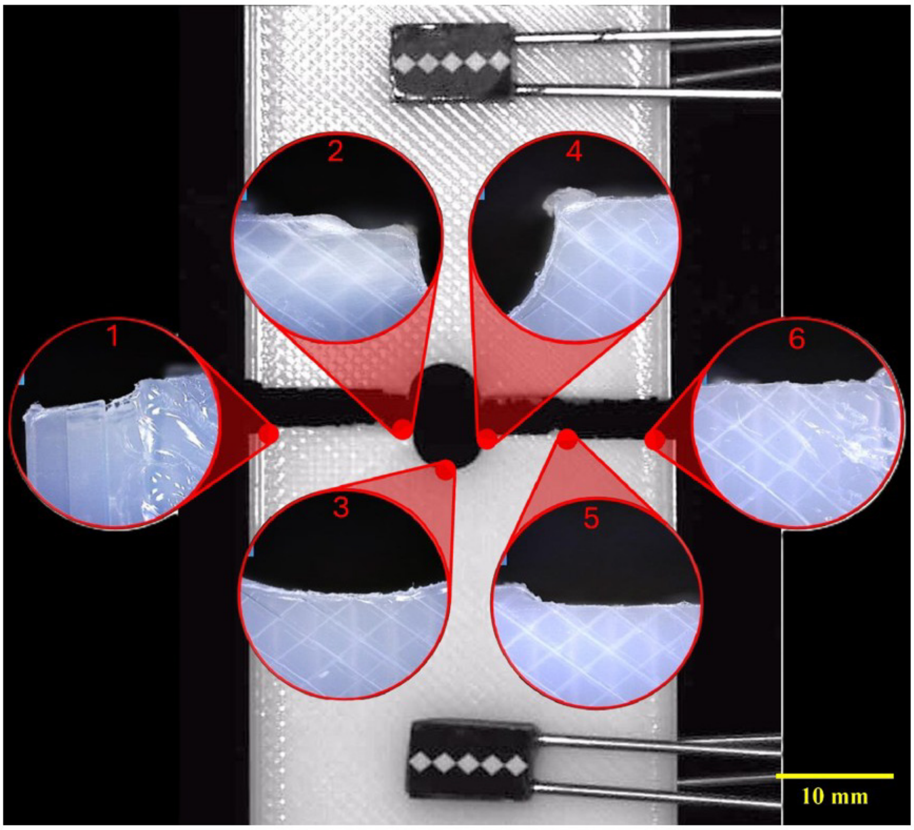

Figure 10 Microscopic image of drilled specimen B1.

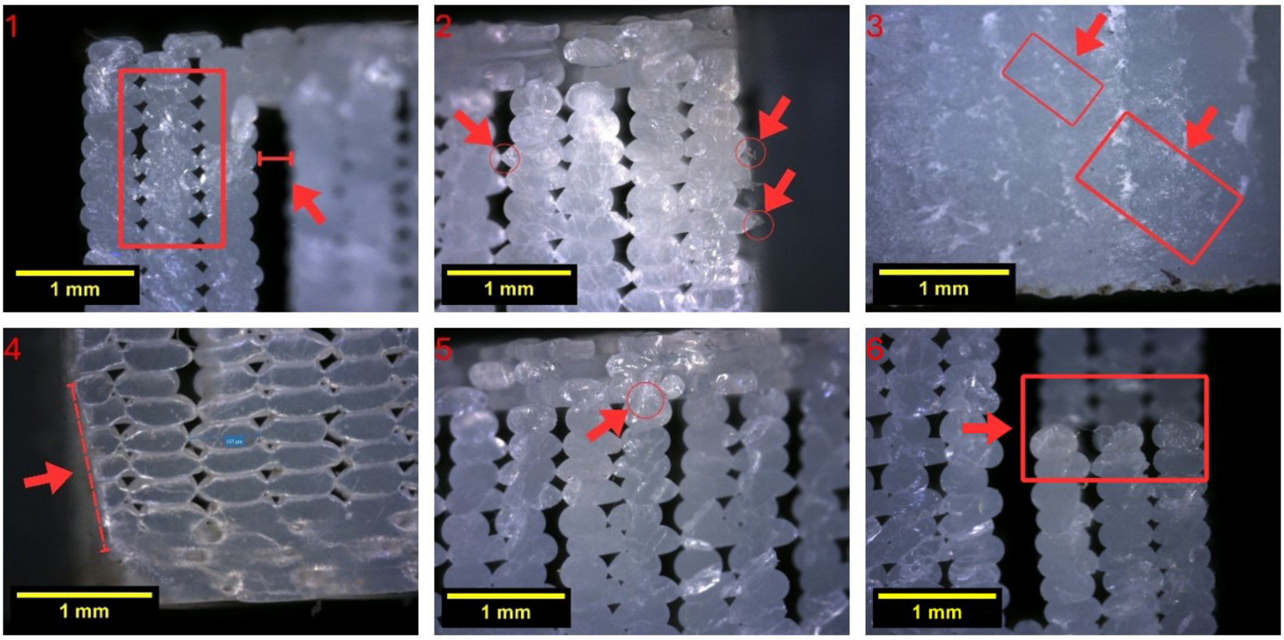

Figure 11 Drilled specimen (B1) showing continuous and well-aligned filament paths around the hole.

In contrast, Figure 12 shows the sequential failure process in a specimen with directly printed holes. As the applied load increased from 2615 N to 5649 N, corresponding to a σ_{nom} range of 18.90–40.85 MPa (calculated from the applied force and cross-sectional area), the crack propagated predominantly along interlayer bonding zones, revealing discontinuities and loss of structural integrity around the hole region.

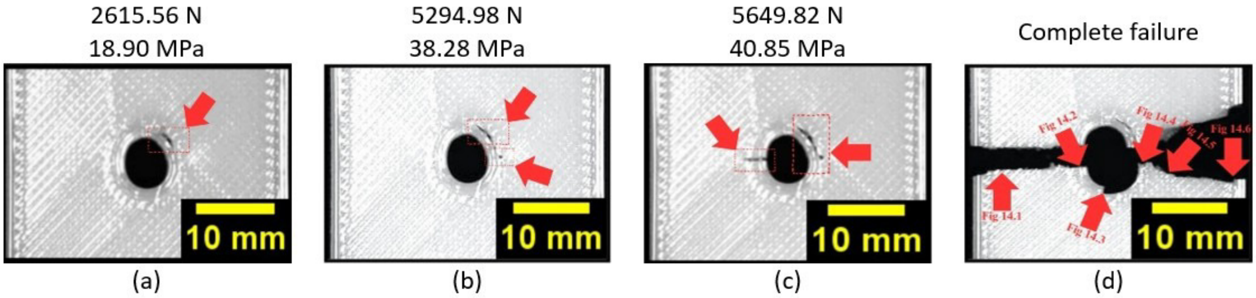

Figure 12 Sequential images showing deformation around the printed hole and crack initiation in a PLA specimen under tensile loading: (a) initial state, (b) micro-void formation near the hole edge, (c) interlayer separation, (d) visible layer disruption and localized deformation.

Figure 12a depicts the initial state without visible cracks, while early stress marks appear near the bottom-right edge of the hole. In Figure 12b, a micro-void forms in the same region, evolving into a visible crack in Figure 12c. The crack continues to expand in Figure 12d, ultimately traversing the narrow section and causing complete specimen failure. The red arrows highlight multiple crack initiation zones and propagation paths.

Microscopic analysis of the B2 series specimens is shown in Figures 13 and 14. Figure 13 provides a macroscopic overview of the printed hole, while Figure 14 reveals significant microscopic defects. In Figure 14, significant delamination, extruded filament interruptions, and burns around the hole edges are visible, suggesting poor bonding. Region 1-3 in Figure 14 demonstrate irregular filament trace orientation and interfacial defects, whereas Region 4-6 illustrates a top-down perspective of the printed-hole geometry, emphasizing the weak shell–infill adhesion. Together, these observations confirm that printed holes promote localized weaknesses and irregular crack propagation compared to drilled specimens, where a more linear and stable failure pattern was observed.

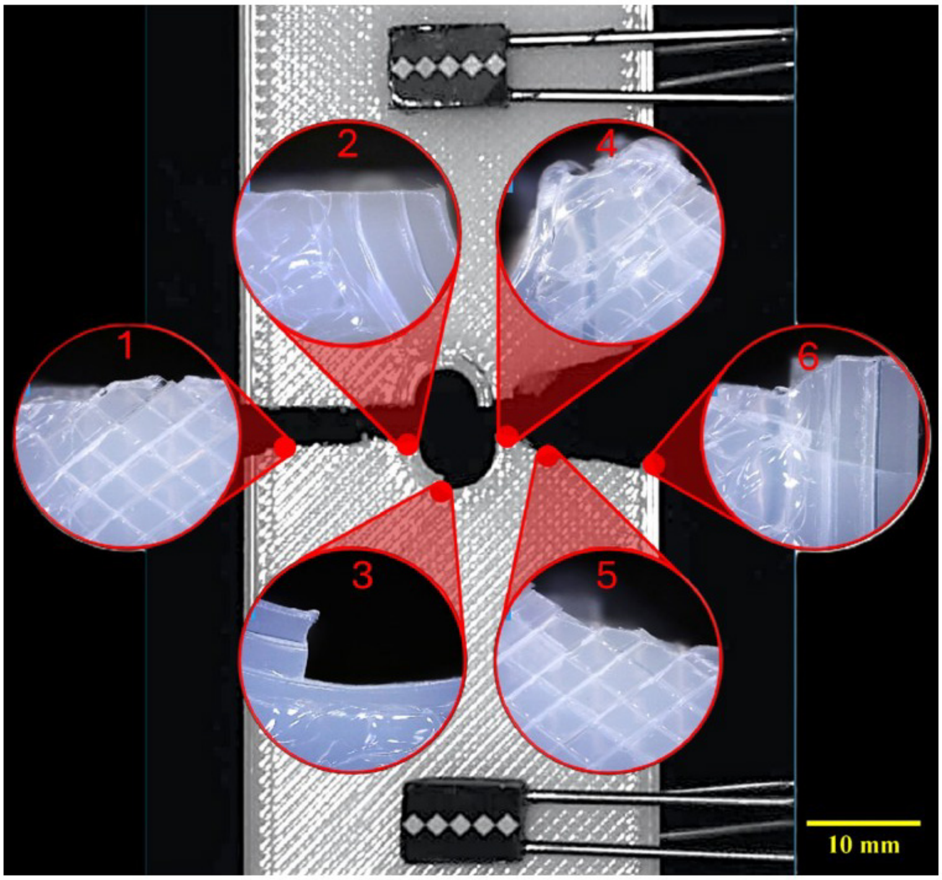

Figure 13 Microscopic image of B2 sample produced with holes.

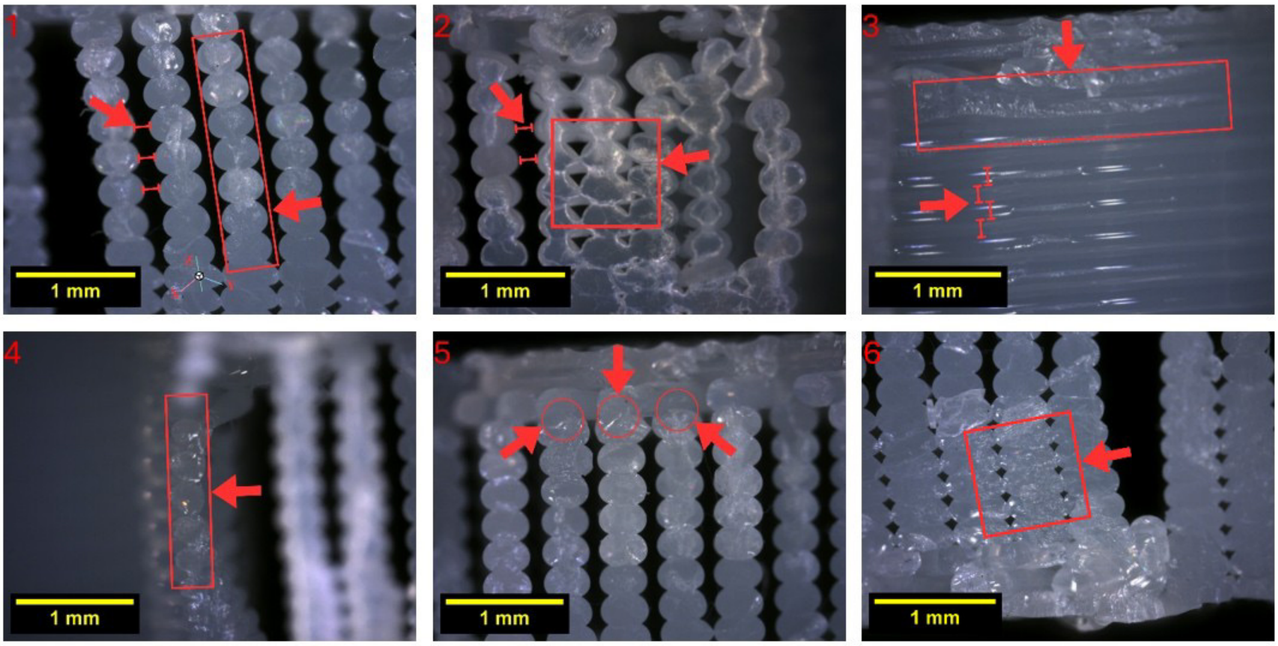

Figure 14 Printed-hole specimen (B2) showing irregular filament path alignment and poor shell–infill bonding.

To further investigate the B2 failure features, Figure 13 provides a cross-sectional overview, complemented by top-down Region in Figure 14. Region 1 shows variations in filament bonding near the outer shell; in contrast, the central region (Region 3) exhibits sound bonding, suggesting spatially heterogeneous damage. Process-induced defects govern the primary failure sites: localized filament disruption at the lower-left edge (Region 2) aligns with the dominant crack path in Figure 12c, while the right edge (Region 4) matches the crack-initiation site in Figure 12b. The shell–infill interface is critical— Region 5 shows the connection of outer shells to the internal structure, and Region 6 the transition zone between them.

2.9. FEA Stress Evolution and Failure Initiation

Overall, the implemented model accurately simulates the deformation behavior of PLA, justifying its use for further numerical analyses involving different geometric configurations and stress concentration scenarios. Figure 15 illustrates the temporal evolution of the equivalent stress distribution in the PLA specimen with a central hole during the tensile simulation. Stress concentration initially emerges around the hole boundary and progressively intensifies, eventually leading to failure. The sequence validates that the implemented MISO accurately captures the stress redistribution and localized plasticity observed in experimental tests.

As validated in Section 2.5 (Figure 5), the model reliably reproduced the stress–strain response. Building on this, Figure 15 illustrates stepwise stress redistribution and failure initiation. Validation focused on the B1 configuration (0° raster, 100% infill, drilled hole), which showed the most stable stress–strain response; other cases are beyond the present scope. Its stable stress–strain profile and minimal manufacturing defects made it a suitable candidate for simulation validation. Extending the numerical study to other configurations was considered beyond the scope of the current validation phase.

The quasi-static nature of the analysis was verified by examining the system's energy balance. As shown in Table 4, the ratio of Kinetic Energy (KE) to Internal Energy (IE) remained negligible (below 1%) throughout the loading phase up to failure initiation, ensuring that inertial effects did not influence the results.

The validity of the simulation was verified by examining the energy balance summarized in Table 4.

Up to $t = 2.50\times10^{-3}$ s (corresponding to the failure initiation observed in Figure 15b), the ratio of kinetic energy (KE) to internal energy (IE) remained well below 1%. This confirms that the stress redistribution and localized plasticity shown in Figure 15a–b represent a valid quasi-static response, unaffected by significant inertial effects.

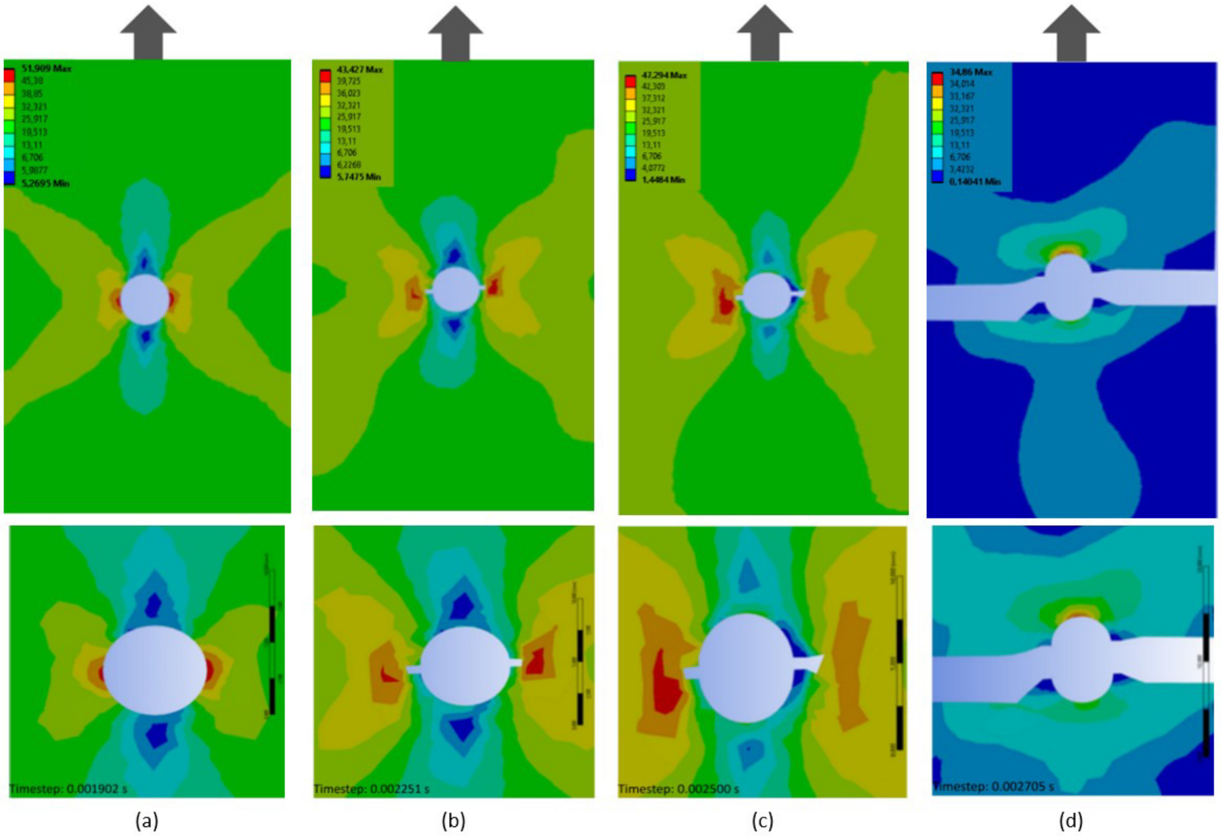

Figure 15. Comparison of von Mises equivalent stress distributions at different time steps for the perforated PLA specimen under displacement-controlled tensile loading (arrow indicates loading direction): (a) initial distribution, (b) onset of localized necking, (c) plastic zone development, (d) failure initiation.

As shown in Table 4, a sharp increase in the KE/IE ratio (≈39.5%) occurs at *t* = 2.75×10^{-3} s, coinciding with the onset of element deletion. This indicates that, beyond this stage, the response is influenced by numerical inertial effects arising from the sudden mass loss.

For this reason, the simulation does not implement a formal progressive damage model. The crack path illustrated in Figure 15c–d was adopted solely for visualization purposes—to demonstrate the likely progression of failure initiation and propagation—rather than to quantitatively predict the exact fracture trajectory observed experimentally.

Table 4 Evolution of internal and kinetic energies during the explicit dynamic analysis.

Time (s)	Internal Energy (mJ)	Kinetic Energy (mJ)
1,18E-38	0,00	0,09
2,50E-04	68,62	6,49
5,00E-04	261,28	12,63
7,50E-04	576,03	20,07
1,00E-03	1024,00	18,56
1,25E-03	1599,00	10,89
1,50E-03	2292,90	2,63
1,75E-03	3107,10	5,29
2,00E-03	4005,30	12,04
2,25E-03	4934,10	8,11
2,50E-03	5887,90	9,68
2,75E-03	3984,50	1575,20
3,00E-03	5643,20	81,23

4 DISCUSSION

The results presented in Section 3 indicate that infill ratio and raster pattern significantly affect the tensile behavior of PLA components manufactured via FFF. Among the tested configurations, specimens fabricated with a 0° raster angle and full infill exhibited the highest strength and rigidity, which appears to stem from the alignment of extruded filament paths along the loading axis, enhancing load-bearing capacity and internal cohesion. The 0° raster / 100% infill configuration was therefore selected as the baseline for subsequent failure analysis (Figure 6 and Figure 7).

A clear difference in behavior was observed between drilled (B1) and printed-hole (B2) specimens, despite their geometrical similarity. On average, B1 samples showed approximately 28% higher values (Figure 8). This trend may be attributed to preserved shell–infill continuity and the absence of significant microstructural defects, as evidenced by microscopic observations (Figures 10–13). In contrast, B2 specimens exhibited signs of interlayer misalignment, delamination, and discontinuous shell transitions, which likely promoted localized stress concentrations and facilitated premature crack initiation (Figures 13–14).

Failure sequence analysis (Figures 9–12) demonstrated that B2 specimens were more prone to premature crack initiation at the hole edge, whereas B1 specimens showed delayed initiation and more stable crack propagation. This distinction highlights the critical role of hole-formation techniques in defining the crack path and overall structural response.

Surface morphology further reinforced this distinction. Drilled specimens (B1) exhibited smooth contours and continuous shell–infill bonding around the hole, while printed-in specimens (B2) showed irregular perimeters, voids, and interlayer misalignments that acted as stress risers and accelerated failure.

Microscopic examination of the failure surfaces reinforces these findings. B1 specimens revealed relatively flat failure planes with sharp transitions and clean filament breakage, while B2 specimens showed more irregular and stepped failure surfaces, including signs of interlayer tearing and pull-out. The morphology of these surfaces therefore suggests a relationship with the observed mechanical performance and highlights the role of microstructural integrity in influencing failure behavior. Similar interpretations have been proposed in prior studies (Pereira et al., 2018; Pilkey et al., 2020)

Another observation relates to the “staircase effect,” a known artifact of FFF, which was especially visible in printed-hole specimens. This effect, as described in more recent studies (Pereira et al., 2018; Matos et al., 2020), arises from the layer-by-layer deposition and introduces geometric irregularities along curved surfaces, sharp micro-edges, and stress intensification. These issues were absent in drilled specimens, supporting claims that subtractive post-processing yields smoother geometries and improved structural consistency (Khosravani and Reinicke, 2022).

The consistency between experimental and simulated results further supports these interpretations. Stress–strain curves obtained from the FEA showed close agreement with test data, particularly in the plastic deformation regime, and mesh sensitivity analysis showed that a 0.5 mm element size offered a reasonable balance between accuracy and computational cost. Importantly, the equivalent stress fields predicted by the model suggested the development of localized plastic zones near the hole edge, consistent with experimentally observed failure initiation.

It is, however, important to recognize the limitations of the numerical model. The MISO formulation employed in the FEA captures ductile plasticity but does not include failure or progressive damage mechanisms. As a result, the simulation is confined to replicating the overall stress–strain response rather than predicting the exact microscopic failure modes. Moreover, the use of an idealized geometry cannot account for process-induced defects such as voids, incomplete fusion, or shell–infill discontinuities. This likely explains why the simulation did not fully reproduce the differences observed between B1 and B2 specimens.

In summary, hole fabrication method strongly affects failure behavior in FFF-PLA. Drilled holes preserved structural integrity, while printed holes introduced discontinuities. This distinction is critical for engineering applications, highlighting that for load-bearing components with stress concentrations, post-processing techniques like drilling should be considered an integral part of the manufacturing workflow rather than an optional step.

5 CONCLUSIONS

This study indicates that the method of hole formation is a primary factor affecting the mechanical response of PLA parts produced by FFF. Across the tested conditions, the 0° raster with 100% infill delivered the highest tensile metrics, which we attribute to the alignment of extruded filament paths and continuous shell–infill bonding along the loading axis. This configuration's combination of high performance and structural consistency made it the ideal baseline, ensuring that differences observed in subsequent failure-focused analyses were under otherwise identical print condition.

Comparing drilled (B1) and printed-in (B2) holes with similar nominal geometry, B1 specimens were associated with higher strength, delayed crack initiation, and a more stable stress-redistribution pattern. Microscopy appeared to support this difference: drilled holes showed smooth contours and uninterrupted shell–infill fusion, whereas printed-in holes exhibited interlayer misalignment, voids, and discontinuous shell transitions that likely acted as stress risers and early crack-initiation sites.

Although the printing-parameter study confirmed that 0°/100% infill optimizes solid-coupon performance, the numerical analyses and classical K_t estimates alone did not reproduce the microstructural differences between B1 and B2. The finite-element model matched the global stress–strain response for an idealized, defect-free specimen, but it does not capture process-induced features (e.g., incomplete fusion) that govern local failure at printed-in holes.

This study's main finding is that the manufacturing method for geometric features is a more critical design parameter for structural reliability than bulk material properties alone. While optimal printing parameters provide a robust material baseline, the results confirm that microstructural integrity—directly governed by the hole-formation technique—is the dominant factor controlling the failure mechanism, not nominal geometric accuracy.

5.1. Limitations of the Study

While the work provides insight into tensile and failure behaviour of FFF-printed PLA, several limitations should be noted.

- **Constitutive model**: The FEA used a MISO model that does not explicitly model failure or progressive delamination; predictions therefore address the global response rather than detailed crack paths.
- **Stress-concentration idealization**: Reported K_t values are based on isotropic formulations and serve as geometric approximations; anisotropy from raster orientation is only indirectly represented.
- **Idealized geometry**: The numerical model assumes a defect-free plate, so process-induced features (voids, incomplete fusion, shell–infill discontinuities) are not represented—likely explaining why differences between drilled and printed-in holes were not fully reproduced.
- **Scope of validation:** Validation is reliable for near-ideal (B1-like) conditions; reduced performance of printed holes, driven by manufacturing defects, lies beyond the current model's predictive scope.

Ultimately, the results underscore that the manufacturing technique for geometric features should be treated as a design parameter: controlling filament bonding and shell–infill continuity—especially near holes—is essential for reliable performance in FFF parts.

Acknowledgements

The authors would like to express their sincere gratitude to the Turkish-German University for providing access to testing equipment and facilities. Special thanks are extended to Assist. Prof. Dr. Ali Can Kaya for his support in enabling the tensile tests at the Mechanical Characterization Laboratory. This study was conducted as part of the PhD research of Enes Kalyoncu under the supervision of Assoc. Prof. Dr. Birgül Aşçıoğlu Temiztaş and Assoc. Prof. Dr. Berna Bolat at Yildiz Technical University.

Author's Contributions: Conceptualization, Enes Kalyoncu; Methodology, Enes Kalyoncu, Birgül Aşçıoğlu Temiztaş and Berna Bolat; Investigation, Enes Kalyoncu; Data curation, Enes Kalyoncu; Formal analysis, Enes Kalyoncu; Software, Enes Kalyoncu; Writing – original draft, Enes Kalyoncu; Visualization, Enes Kalyoncu; Writing – review & editing, Birgül Aşçıoğlu Temiztaş and Berna Bolat, Ali Can Kaya; Supervision, Birgül Aşçıoğlu Temiztaş and Berna Bolat; Resources, Birgül Aşçıoğlu Temiztaş and Ali Can Kaya; Technical support, Ali Can Kaya.

Data Availability statement: The data supporting the findings of this study are presented in the figures and tables within the article and in the supplementary material. Raw data are available from the corresponding author upon reasonable request.

Editor: Pablo Andrés Muñoz Rojas

References

Abeykoon, C., Sri-Amphorn, P., & Fernando, A. (2020). Optimization of fused deposition modeling parameters for improved PLA and ABS 3D printed structures. International Journal of Lightweight Materials and Manufacture, 3(3), 284-297. https://doi.org/10.1016/j.ijlmm.2020.03.003

Aftab, M., Ikram, S., Ullah, M., Khan, N., Naeem, M., Khan, M. A., ... & Qizi, O. K. A. (2025). Recent Trends and Future Directions in 3D Printing of Biocompatible Polymers. Journal of Manufacturing and Materials Processing, 9(4), 129. https://doi.org/10.3390/jmmp9040129

Akhoundi, B., & Behravesh, A. H. (2019). Effect of filling pattern on the tensile and flexural mechanical properties of FDM 3D printed products. Experimental Mechanics, 59, 883-897. https://doi.org/10.1007/s11340-018-00467-y

Albadrani, M. A. (2023). Effects of Raster Angle on the Elasticity of 3D-Printed Polylactic Acid and Polyethylene Terephthalate Glycol. *Designs, 7*(5), 112 https://doi.org/10.3390/designs7050112

Anand Kumar, S., & Shivraj Narayan, Y. (2018). Tensile testing and evaluation of 3D-printed PLA specimens as per ASTM D638 type IV standard. In Innovative Design, Analysis and Development Practices in Aerospace and Automotive Engineering (I-DAD 2018) Volume 2 (pp. 79-95). Springer Singapore. https://doi.org/10.1007/978-981-13-2718-6_9

ASTM D5766, (2019). “ASTM D5766 Standard Test Method for Open Hole Tensile Strength of Polymer Matrix Composite Laminates,” ASTM B. Stand., vol. 03, pp. 2–7. https://doi.org/10.1520/D5766_D5766M-11R18

ASTM D638, (2016). “ASTM D638-14, Standard practice for preparation of metallographic specimens,” ASTM B. Stand., vol. 82, no. C, pp. 1–15. https://doi.org/10.1520/D0638-14.1

Badiru, A. B. (2017). From traditional manufacturing to additive manufacturing. In Additive Manufacturing Handbook CRC Press, 2017. p. 3-30.

Bergonzi, L., Pirondi, A., Moroni, F., Frascio, M., & Avalle, M. (2024). A study on additive manufacturing build parameters as bonded joint design factors. The Journal of Adhesion, 100(5), 576–605. https://doi.org/10.1080/00218464.2020.1862655

Brounstein, Z., Talley, S., Dumont, J. H., Zhao, J., Lee, K. S., & Labouriau, A. (2020). Fused filament fabrication of polymer composites for extreme environments. Journal of Materials Research, 35(12), 1493-1503. https://doi.org/10.1557/jmr.2020.118

Chokshi, H., Shah, D. B., Patel, K. M., & Joshi, S. J. (2022). Experimental investigations of process parameters on mechanical properties for PLA during processing in FDM. Advances in Materials and Processing Technologies, 8(sup2), 696-709. https://doi.org/10.1080/2374068X.2021.1946756

Choudary, R., Saini, N., Chopra, D. S., Singh, D., & Singh, N. (2023). A comprehensive review of 3D bioprinting biomaterials: Properties, strategies and wound healing application. Journal of Materials Research, 38(13), 3264-3300. https://doi.org/10.1557/s43578-023-01078-7

Dave, H. K., Prajapati, A. R., Rajpurohit, S. R., Patadiya, N. H., & Raval, H. K. (2020). Open hole tensile testing of 3D printed parts using in-house fabricated PLA filament. Rapid Prototyping Journal, 26(1), 21-31. https://doi.org/10.1108/RPJ-01-2019-0003

Dai, S., Deng, Z. C., Yu, Y. J., Zhang, K., Wang, S. H., & Ye, J. (2020). Orthotropic elastic behaviors and yield strength of fused deposition modeling materials: Theory and experiments. *Polymer Testing, 87*, 106520 https://doi.org/10.1016/j.polymertesting.2020.106520

dos Santos, W. F., Ferreira, A. R., & Proença, S. P. B. (2022). Complete geometric representation of yield surfaces for porous ductile media by a 3D computational homogenization approach: an assessment of the Gurson yield criterion. Journal of the Brazilian Society of Mechanical Sciences and Engineering, 44(1), 163. https://doi.org/10.1007/s40430-022-03483-1

Farah, S., Anderson, D. G., & Langer, R. (2016). Physical and mechanical properties of PLA, and their functions in widespread applications—A comprehensive review. Advanced drug delivery reviews, 107, 367-392. https://doi.org/10.1016/j.addr.2016.06.012

Guessasma, S., & Belhabib, S. (2022). Infill strategy in 3D printed PLA carbon composites: effect on tensile performance. Polymers, 14(19), 4221. https://doi.org/10.3390/polym14194221

Khosravani, M. R., & Reinicke, T. (2022). Mechanical strength of 3D-printed open hole polymer plates. Procedia Structural Integrity, 41, 664-669. https://doi.org/10.1016/j.prostr.2022.05.075

Khosravani, M. R., Božić, Ž., Zolfagharian, A., & Reinicke, T. (2022). Failure analysis of 3D-printed PLA components: Impact of manufacturing defects and thermal ageing. Engineering Failure Analysis, 136, 106214. https://doi.org/10.1016/j.engfailanal.2022.106214

Kim, S. W., Cha, M. C., Lee, I., Kim, E. H., Kwon, I. B., & Hwang, T. K. (2014). Damage evaluation and strain monitoring of composite plates using metal-coated FBG sensors under quasi-static indentation. *Composites Part B: Engineering, 66*, 36-45. https://doi.org/10.1016/j.compositesb.2014.03.012

Laureto, J. J., & Pearce, J. M. (2018). Anisotropic mechanical property variance between ASTM D638-14 type i and type iv fused filament fabricated specimens. *Polymer Testing, 68*, 294-301 https://doi.org/10.1016/j.polymertesting.2018.04.029

Lipton, J. I., Cutler, M., Nigl, F., Cohen, D., & Lipson, H. (2015). Additive manufacturing for the food industry. Trends in food science & technology, 43(1), 114-123. https://doi.org/10.1016/j.tifs.2015.02.004

Li, M., Xu, Y., & Fang, J. (2024). Orthotropic mechanical properties of PLA materials fabricated by fused deposition modeling. *Thin-Walled Structures, 199*, 111800 https://doi.org/10.1016/j.tws.2024.111800

Liu, Z., Wang, Y., Wu, B., Cui, C., Guo, Y., & Yan, C. (2019). A critical review of fused deposition modeling 3D printing technology in manufacturing polylactic acid parts. The International Journal of Advanced Manufacturing Technology, 102, 2877-2889. https://doi.org/10.1007/s00170-019-03332-x

Lorkowski, L., Wybrzak, K., Brancewicz-Steinmetz, E., Świniarski, J., & Sawicki, J. (2025). Influence of Print Speed on the Mechanical Performance of 3D-Printed Bio-Polymer Polylactic Acid. Materials, 18(8), 1765. https://doi.org/10.3390/ma18081765

Love, L. J., Kunc, V., Rios, O., Duty, C. E., Elliott, A. M., Post, B. K., ... & Blue, C. A. (2014). The importance of carbon fiber to polymer additive manufacturing. Journal of Materials Research, 29(17), 1893-1898. https://doi.org/10.1557/jmr.2014.212

Lubombo, C., & Huneault, M. A. (2018). Effect of infill patterns on the mechanical performance of lightweight 3D-printed cellular PLA parts. Materials Today Communications, 17, 214-228. https://doi.org/10.1016/j.mtcomm.2018.09.017

Luo, G., Mo, D., Chai, C., Liu, J., & Chen, Y. (2023). Mechanical and energy-absorption properties of a 3D-printed star-shaped auxetic honeycomb under combined compression-shear loading. Latin American Journal of Solids and Structures, 20(3), e486. https://doi.org/10.1590/1679-78257624

Matos, M. A., Rocha, A. M. A., & Pereira, A. I. (2020). Improving additive manufacturing performance by build orientation optimization. *The International Journal of Advanced Manufacturing Technology, 107*(5), 1993-2005. https://doi.org/10.1007/s00170-020-04942-6

Mira, J. B., Restrepo, V., Vajipeyajula, B., & Patterson, A. E. (2024). Impact of compact tension specimen size on failure toughness of FFF-processed thermoplastics. Procedia Structural Integrity, 61, 156-163. https://doi.org/10.1016/j.prostr.2024.06.021

Mohamed, O. A., Masood, S. H., & Bhowmik, J. L. (2015). Optimization of fused deposition modeling process parameters: a review of current research and future prospects. Advances in manufacturing, 3, 42-53. https://doi.org/10.1007/s40436-014-0097-7

Moradi, M., Rezayat, M., Rozhbiany, F. A. R., Meiabadi, S., Casalino, G., Shamsborhan, M., ... & Karamimoghadam, M. (2023). Correlation between infill percentages, layer width, and mechanical properties in fused deposition modelling of poly-lactic acid 3D printing. Machines, 11(10), 950. https://doi.org/10.3390/machines11100950

Pereira, S., Vaz, A. I. F., & Vicente, L. N. (2018). On the optimal object orientation in additive manufacturing. *The International Journal of Advanced Manufacturing Technology, 98*(5), 1685-1694. https://doi.org/10.1007/s00170-018-2218-0

Pilkey, W. D., Pilkey, D. F., & Bi, Z. (2020). Peterson's stress concentration factors. John Wiley & Sons. https://doi.org/10.1002/9781119532552

Rafiee, R., Amohaji, H., & Khezma, H. (2025). Estimating Strength of 3D-Printed Polymers Based on the Appraisal of Available Methods. Journal of Materials Engineering and Performance, 1-11. https://doi.org/10.1007/s11665-025-10880-9

Raj, S. A., Muthukumaran, E., & Jayakrishna, K. (2018). A case study of 3D printed PLA and its mechanical properties. Materials Today: Proceedings, 5(5), 11219-11226. https://doi.org/10.1016/j.matpr.2018.01.146

Solomon, I. J., Sevvel, P., & Gunasekaran, J. J. M. T. P. (2020). A review on the various processing parameters in FDM. Materials Today: Proceedings, 37, 509-514. https://doi.org/10.1016/j.matpr.2020.05.484

Szczepanik, S., & Nikiel, P. (2020). Influence of structural characteristics on the mechanical properties of FDM printed PLA material. Journal of Casting & Materials Engineering, 4(1), 1-8. https://doi.org/10.7494/jcme.2020.4.1.1

Talagani, M. R., DorMohammadi, S., Dutton, R., Godines, C., Baid, H., Abdi, F., ... & Blue, C. (2015). Numerical simulation of big area additive manufacturing (3D printing) of a full-size car. SAMPE J, 51(4), 27-36.

Tanveer, M. Q., Mishra, G., Mishra, S., & Sharma, R. (2019). Effect of infill pattern and infill density on mechanical behaviour of FDM 3D printed Parts-a current review. Materials Today: Proceedings, 62, 100-108. https://doi.org/10.1016/j.matpr.2022.02.310

Triyono, J., Sukanto, H., Saputra, R. M., & Smaradhana, D. F. (2020). The effect of nozzle hole diameter of 3D printing on porosity and tensile strength parts using polylactic acid material. Open Engineering, 10(1), 762-768. https://doi.org/10.1515/eng-2020-0083

W. C. Young and R. G. Budynas, (2002) Roark's Formulas for Stress and Strain. 7th Edition, McGraw-Hill, New York.

Yao, T., Deng, Z., Zhang, K., & Li, S. (2019). A method to predict the ultimate tensile strength of 3D printing polylactic acid (PLA) materials with different printing orientations. Composites Part B: Engineering, 163, 393-402. https://doi.org/10.1016/j.compositesb.2019.01.025

Yao, T., Ye, J., Deng, Z., Zhang, K., Ma, Y., & Ouyang, H. (2020). Tensile failure strength and separation angle of FDM 3D printing PLA material: Experimental and theoretical analyses. Composites Part B: Engineering, 188, 107894. https://doi.org/10.1016/j.compositesb.2020.107894

Zhao, Y., Chen, Y., & Zhou, Y. (2019). Novel mechanical models of tensile strength and elastic property of FDM AM PLA materials: Experimental and theoretical analyses. Materials & Design, 181, 108089. https://doi.org/10.1016/j.matdes.2019.108089